Geophysical Research Letters

RESEARCH LETTER
10.1029/2022GL099580

Autocorrelation R_2 on Mars

Sizhuang Deng[1] and Alan Levander[1]

[1]Department of Earth, Environmental and Planetary Sciences, Rice University, Houston, TX, USA

Key Points:

- The R_2 surface waves on Mars are recovered by low-frequency ambient noise autocorrelation of Interior Exploration Using Seismic Investigations, Geodesy and Heat Transport (InSight) seismic data
- An updated upper mantle velocity model is developed using a Monte Carlo method to fit the observed R_2 surface waves on Mars
- The S-wave low velocity zone extends to ~400 km depth, consistent with the results from previous studies

Supporting Information:

Supporting Information may be found in the online version of this article.

Correspondence to:

S. Deng,
sd62@rice.edu

Citation:

Deng, S., & Levander, A. (2022). Autocorrelation R_2 on Mars. *Geophysical Research Letters*, *49*, e2022GL099580. https://doi.org/10.1029/2022GL099580

Received 17 MAY 2022
Accepted 5 SEP 2022

Author Contributions:

Conceptualization: Sizhuang Deng, Alan Levander
Data curation: Sizhuang Deng
Formal analysis: Sizhuang Deng
Funding acquisition: Alan Levander
Investigation: Sizhuang Deng
Methodology: Sizhuang Deng
Project Administration: Alan Levander
Resources: Sizhuang Deng, Alan Levander
Software: Sizhuang Deng
Supervision: Alan Levander
Validation: Sizhuang Deng
Visualization: Sizhuang Deng
Writing – original draft: Sizhuang Deng
Writing – review & editing: Sizhuang Deng, Alan Levander

Abstract A purpose of the Interior Exploration Using Seismic Investigations, Geodesy and Heat Transport (InSight) mission is to reveal the Martian interior structure with seismic data. In this work, ambient noise autocorrelation of the continuously recorded vertical-component seismic signals has extracted the Rayleigh waves that propagate around Mars for one cycle, R_2. The Mars orbiting surface waves are observed at a lag time of ~6,000 s in the stacked autocorrelation series filtered between 0.005 and 0.01 Hz. Synthetic seismograms from a set of radially concentric velocity models were computed to find the best-fitting one as the starting model for a Monte Carlo inversion. The starting model was randomly perturbed iteratively to increase the correlation coefficients and reduce the absolute time shifts between the synthetic and observed R_2. An S-wave low-velocity layer in the inverted velocity model extends to ~400 km depth, consistent with Marsquake observations, geophysical inversion, and high-pressure experiments.

Plain Language Summary The subsurface structures of Earth are imaged by the detailed analysis of seismic data recorded by thousands of stations deployed on the Earth's surface. The Interior Exploration Using Seismic Investigations, Geodesy and Heat Transport (InSight) mission landed a seismograph on Mars, which was deployed at the end of 2018 to investigate the planet's interior structure and dynamic evolution. In this study, we preprocessed the continuous vertical-component seismic data, and by autocorrelation retrieved a Rayleigh wave, one class of seismic surface wave, that orbits Mars. Rayleigh wave group velocities between 115 and 200 s period were measured from the observed Mars orbiting Rayleigh waves. Synthetic seismograms were calculated using current estimates of the velocity structure of Mars for comparisons to the observation. The spherically symmetric model was updated with a Monte Carlo algorithm, an inversion method that randomly perturbs the velocity model and determines the model that best matches the Mars orbiting surface waves through trial and error. An S-wave low-velocity zone is observed to the depth of ~400 km beneath the Martian surface, consistent with other InSight seismic observations and velocity models measured from geophysical modeling and high-pressure laboratory experiments.

1. Introduction

The InSight (Interior Exploration Using Seismic Investigations, Geodesy and Heat Transport) spacecraft landed on Mars on 26 November 2018 and installed the seismograph SEIS (Seismic Experiment for Interior Structure) (Lognonné et al., 2019) to record continuous seismic data for approximately 3 years, providing opportunities to investigate another terrestrial planet's interior. A variety of research studies have been conducted recently to analyze the seismic recordings on Mars to monitor the seismicity (Banerdt et al., 2020; Böse et al., 2021; Ceylan et al., 2021; Clinton et al., 2021; Giardini et al., 2020; Knapmeyer et al., 2021), understand the ambient noise characteristics (Stutzmann et al., 2021; Suemoto et al., 2020) and recover the subsurface structures (Compaire et al., 2021; Deng & Levander, 2020; Khan et al., 2021; Knapmeyer-Endrun et al., 2021; J. Li et al., 2022; Lognonné et al., 2020; Schimmel et al., 2021; Stähler et al., 2021). A prominent reflection phase is observed at ~11 s in the stacked ambient noise autocorrelations, which may correspond to the crust-mantle boundary (Moho) or a mid-crust discontinuity at ~35 km (Compaire et al., 2021; Deng & Levander, 2020; Schimmel et al., 2021) and is consistent with the shallow velocity models derived from receiver function analysis (Knapmeyer-Endrun et al., 2021; Lognonné et al., 2020; Schimmel et al., 2021). Moving to the deeper interior of Mars, the core-reflected phases (e.g., PcP and ScS) are observed from the Marsquake recordings (Stähler et al., 2021) and ambient noise autocorrelations (Deng & Levander, 2020), where the radius of Martian core is estimated as ~1,830 km for both methods (Deng & Levander, 2020; Stähler et al., 2021). However, some researchers have suggested that the observation of the PcP phase (Deng & Levander, 2020) may originate from the quasi periodic seismic glitches in the continuous SEIS data (Barkaoui et al., 2021; Kim et al., 2021). We comment on this in another manuscript.

Seismic interferometry has been widely applied to retrieve the empirical Green's functions of surface waves (Berg et al., 2018; Miao et al., 2022; Qiu et al., 2020, 2021; Schimmel et al., 2018; Shen et al., 2013; Yao et al., 2006) and body waves (Clayton, 2020; Feng et al., 2017, 2021; Gorbatov et al., 2013; Kennett, 2015; Oren & Nowack, 2017; She et al., 2022) from ambient noise auto- and cross-correlations. Many ambient noise surface wave tomography studies on Earth have focused on the calculations of the Rayleigh wave phase velocity to invert for the S-wave velocity of sedimentary basins (Cai et al., 2022; Hannemann et al., 2014; Pan et al., 2016; Qiu et al., 2019; Shirzad & Shomali, 2014), the crust and upper mantle (Li et al., 2012; Lin et al., 2014; Nguyen et al., 2022; Yao et al., 2008; Zhang et al., 2018). Global tomography analysis suggested that the long period Rayleigh waves (e.g., >100 s) can be recovered by cross-correlations of the Earth's hum (Haned et al., 2016; Nishida et al., 2009). This was subsequently extended to extract the Earth orbiting Rayleigh waves from a single-station-based autocorrelation to constrain the upper mantle velocity models (Li et al., 2020; J. Xie & Ni, 2019; Schimmel et al., 2018).

The observation of Rayleigh waves traveling around the Earth once, the phase R_2, using low-frequency autocorrelation of background free oscillations suggests the potential for a similar analysis for InSight seismic data (Schimmel et al., 2018), which then can be used to constrain Martian upper mantle velocity structure (J. Xie & Ni, 2019). Here, we followed the processing procedures in Bensen et al. (2007) to compute and stack the vertical-component autocorrelograms of the SEIS ambient noise data, which were band-pass filtered from 0.005 to 0.01 Hz to retrieve the R_2 surface waves. The group dispersion curves were extracted by frequency-time analysis (FTAN) (Bensen et al., 2007; Levshin et al., 1992). We then compared observed R_2 to synthetic R_2 waveforms calculated from a suite of 1-D velocity models developed previously from joint inversion of multiple geophysical data types (Stähler et al., 2021). The best fit model from the Stähler et al. (2021) suite of models was used as the starting 1D model in a Monte Carlo inversion. We iteratively adjusted the Martian upper mantle velocity model between 40 and 700 km depth to minimize the misfit between synthetic R_2 waveforms and the stacked R_2 autocorrelation.

2. Data and Methods

2.1. Martian Seismic Data and Glitch Removal

The InSight broadband continuous seismic data (InSight Mars SEIS Data Service, 2019) were obtained from the IRIS (Incorporated Research Institutions for Seismology) website in three nonorthogonal channels (U-V-W). The data were sampled at 10 Hz between February and May 2019 and at 20 Hz between June 2019 and March 2021. The raw continuous signals contain the repeated high-amplitude glitches primarily induced by the stress relaxation of the seismometer (Scholz et al., 2020), which may contaminate ambient noise autocorrelations (Compaire et al., 2021; Kim et al., 2021). In order to mitigate the effects of these high-amplitude spikes, we applied the open-source Python package SEISglitch (Scholz et al., 2020) to detect and remove the quasi-periodic glitches in the raw SEIS data. Figure S1 in Supporting Information S1 compares a 1-day record of the original and deglitched U-V-W components; the deglitched waveforms are clearly less spiky than the raw continuous data. We performed tests to determine that the glitch removal method can mitigate the effects of glitches without introducing additional artifacts (Figures S2 and S3 in Supporting Information S1). The instrument responses were deconvolved from the deglitched continuous waveforms, and the data were then band-pass filtered from 0.002 to 3.5 Hz. The data with a 20 Hz sampling rate were downsampled to 10 Hz. We cut the ambient noise data into 584 daily segments and then rotated them to the orthogonal vertical, north and east (Z-N-E) components according to the azimuthal and dip angles of the oblique U-V-W components (Compaire et al., 2021; Suemoto et al., 2020). For each 1-day ambient noise epoch, the mean and linear trend were removed, and a 5% cosine tapered window was applied. We also computed and stacked the autocorrelations using 12-hr epochs (Figure S4 in Supporting Information S1) to demonstrate the robustness of phase identification.

2.2. Calculating and Stacking Autocorrelations

Before the calculation of autocorrelograms, we applied temporal balance and spectral whitening, implemented with the running-absolute-mean normalization method in the time and frequency domains (Bensen et al., 2007), to remove the effects of non-stationary signals in the daily continuous data. The daily autocorrelograms were computed by the inverse Fourier transform of the power spectra of the vertical-component ambient noise signals bandpass filtered from 0.005 to 0.01 Hz and normalized to the zero-lag value. The root mean square ratio selection

(RMSR_S) was used to remove epochs with non-stationary phases (J. Xie et al., 2020), resulting in a reduction of the data set by 9%–15% depending on window parameters chosen (Text S2 and Figure S5 in Supporting Information S1). Details of RMSR_S are described in Text S2 in Supporting Information S1. The signal window was selected as 5,600–6,400 s and the noise window as 4,800–5,500 s. The threshold value G for RMSR_S was set as 1.02. After the application of RMSR_S, 508 autocorrelation functions from a total of 584, that is, 87%, were included in the final stack. Figure S5 in Supporting Information S1 shows tests of different signal and noise window selections in RMSR_S and the corresponding binary a^k values. The tests give almost identical results. Finally, the daily autocorrelograms were stacked to retrieve R_2 surface waves using both linear stacking (LS) and time-frequency domain phase-weighted stacking (tf-PWS) (G. Li et al., 2018; Schimmel & Gallart, 2007). In this study, we empirically chose the power of tf-PWS as 2, which is a common selection for Earth data analysis (Hable et al., 2019; Haned et al., 2016; Schimmel et al., 2011; Yan et al., 2019; Zeng et al., 2017). Figure S6 in Supporting Information S1 shows tests for different exponents in the tf-PWS. Figure S7 in Supporting Information S1 is a synthetic test designed to demonstrate the efficiency of tf-PWS to enhance coherent signals.

3. Results and Discussion

3.1. Autocorrelation Results of R_2 Surface Waves

A signal that we interpret as the Mars orbiting Rayleigh wave R_2 is prominent at ~6,000 s in the vertical-component ambient noise autocorrelations filtered between 0.005 and 0.01 Hz with both linear (Figures 1a and 1b) and tf-PWS stacking (Figures 1c and 1d). With the application of RMSR_S (J. Xie et al., 2020), the R_2 signal is more prominent (Figures 1e–1h). Bootstrap calculations using a subset of the whole data set further suggest the R_2 phase identification is robust (Figure S8 in Supporting Information S1). In the following, we applied FTAN (Bensen et al., 2007; Levshin et al., 1992) to calculate the group velocities between 115 and 200 s (Figures 2b and S9 in Supporting Information S1) for the stacked waveform using both RMSR_S and tf-PWS (Figure 1h) and compared these with the synthetic group dispersion curves of several Martian 1-D velocity models (Figure 2a; Stähler et al., 2021). Synthetic R_2 seismograms were also generated to compare with the observed R_2 waveform in Figure 1h (Figure 2c).

3.2. Comparison With the Synthetic Group Dispersion Curves and Seismograms

We calculated synthetic group velocity dispersion curves for a set of velocity models (Figure 2a) derived from a probabilistic inversion to fit the tidal Love number k_2, moment of inertia and seismic traveltimes (Stähler et al., 2021) for comparisons to the group velocities (Figure 2b) derived from the stacked autocorrelation in Figure 1h. The FTAN-measured group velocities are compatible with the velocity model 3 standard deviations lower than the mean velocity of Stähler et al. (2021) (Figure 2b).

The R_2 Rayleigh waves can travel along any or all great circle paths on the Martian surface and possess travel distances that vary due to the planet's ellipticity ($\varepsilon = 0.00589$) (J. Xie & Ni, 2019). J. Xie and Ni (2019) discussed the effects of ellipticity on the group velocity estimation of the Earth's orbiting surface waves, concluding that the effects are negligible. Accounting for the travel distance variations of R_2 surface waves, we simulated and then calculated a weighted mean of the synthetic Green's functions for a range of radii between the polar and equatorial radius (3,376.2–3,396.2 km) using the direct solution method (DSM) software (Geller & Takeuchi, 1995; Kawai et al., 2006; Takeuchi et al., 1996). The mean synthetic was almost identical to the synthetic Green's functions using the mean Martian radius (3,389.5 km) (Figure S10 in Supporting Information S1). The synthetic Green's functions were then convolved with a source wavelet (Figure S11 in Supporting Information S1), estimated from the second zero-crossing of the side lobes of the autocorrelation near zero-lag (Erhan & Nowack, 2020; Yilmaz, 2001), to produce the synthetic R_2 seismograms.

We generated synthetic seismograms for the velocity models (Figure 2a) for comparisons to Figure 1h (Figure 2c). The time lag indicated in Figure 2c is the cross-correlation time shift between the observed R_2 (Figure 1h) and each individual synthetic seismogram, where positive values correspond to the traveltime delays of the observed R_2 Rayleigh waves. The time lags are positive for velocity models from 3 standard deviations above the mean to 2 standard deviations lower than the mean velocity, and change sign at 3 standard deviations lower (Figure 2c). The waveform comparison (Figure 2c) also suggests that the upper mantle velocity model of Mars may be slightly slower on average than predicted by the mean value of the Stähler et al. (2021) model.

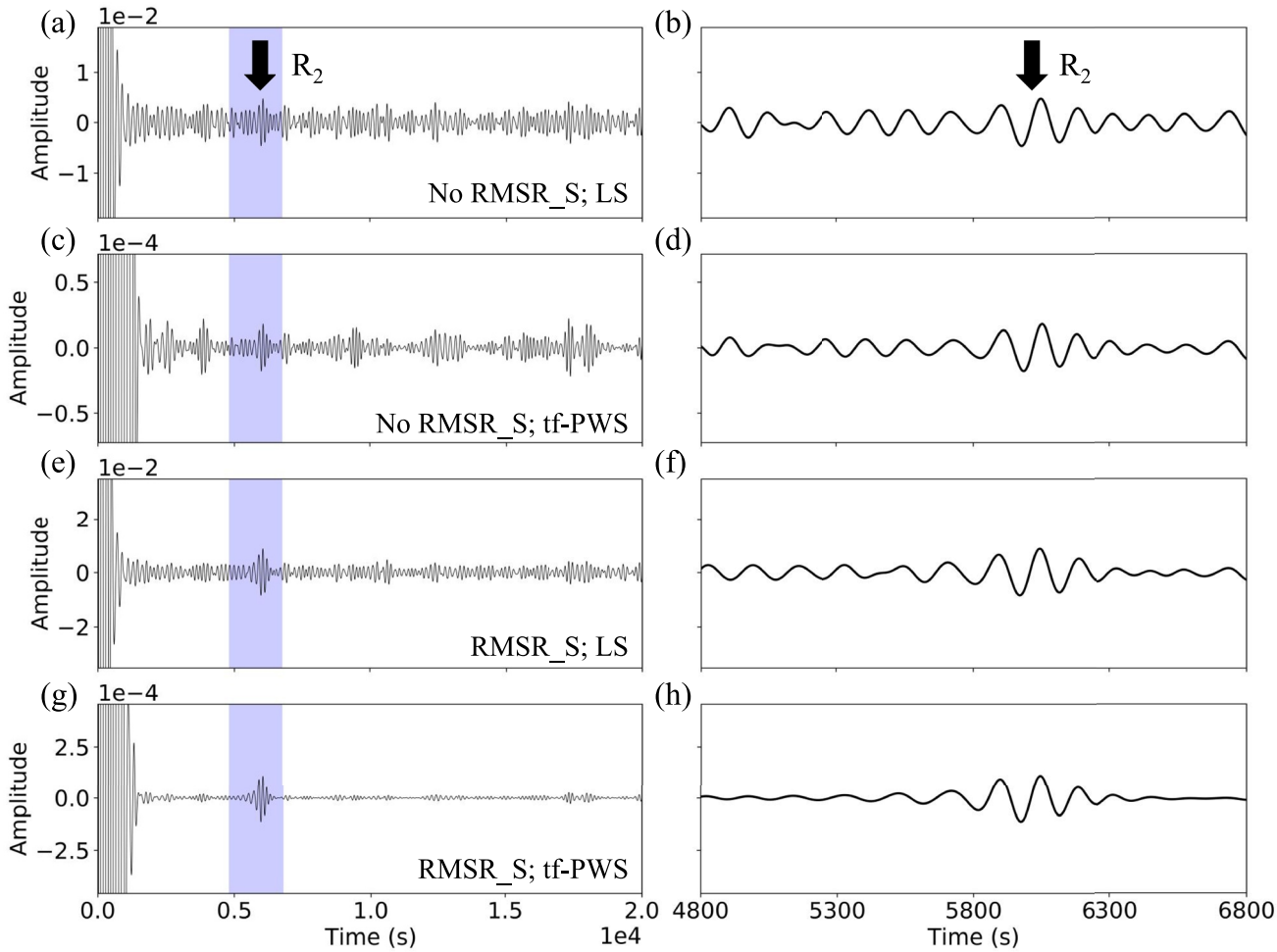

Figure 1. (a) Linearly stacked (LS) autocorrelation filtered between 0.005 and 0.01 Hz without the application of root mean square ratio selection (RMSR_S). (b) The R_2 signal of (a) between 4,800 and 6800 s (blue-shaded area in (a)). (c) Same as (a) but applying time-frequency domain phase-weighted stacking (tf-PWS). (d) The R_2 signal of (c) between 4,800 and 6,800 s (blue-shaded area in (c)). (e) Same as (a) but applying RMSR_S. (f) The R_2 signal of (e) between 4,800 and 6800 s (blue-shaded area in (e)). (g) Same as (e) but applying tf-PWS. (h) The R_2 signal of (g) between 4,800 and 6,800 s (blue-shaded area in (g)). The stacked autocorrelation in (g, h) shows the most prominent R_2 signal and is used to compare with the synthetic results. After the application of RMSR_S, 508 autocorrelation functions among total 584 were maintained for the final stack.

3.3. Monte Carlo Inversion for the Martian Upper Mantle Velocity

We employed a Monte Carlo inversion in which we perturbed the velocity in the depth range from 40 to 700 km, as suggested by the Rayleigh wave sensitivity kernels (Figure S12 in Supporting Information S1), to better constrain the upper mantle seismic structures of Mars. For the starting model, we chose the velocity model from Stähler et al. (2021) that produced the best fit to the observation (Figure 1h): This was the model 3σ lower than the mean velocity (Figures 2b and 2c). For each iteration, we randomly perturbed the starting velocity model 10 times and calculated the DSM (Kawai et al., 2006) synthetic seismograms for these 10 new velocity models. We next computed the correlation time shifts and correlation coefficients between the observed R_2 (Figure 1h) and the synthetic R_2 waveforms of these 10 models. The model with the smallest absolute correlation time shifts and highest correlation coefficients was used for the next iteration. We repeated the same procedure for three iterations since the misfit increased upon further perturbation of the velocity model.

Figures 3a and 3b show the upper mantle P- and S-wave velocity model update during each iteration of the Monte Carlo inversion and the right four panels (Figures 3c–3f) illustrate the comparisons between the observed R_2 (Figure 1h) and the synthetic seismograms of the best model in each iteration. Compared to the starting model, the final upper mantle velocity model after three iterations (black model in Figures 3a and 3b; Table S1 in

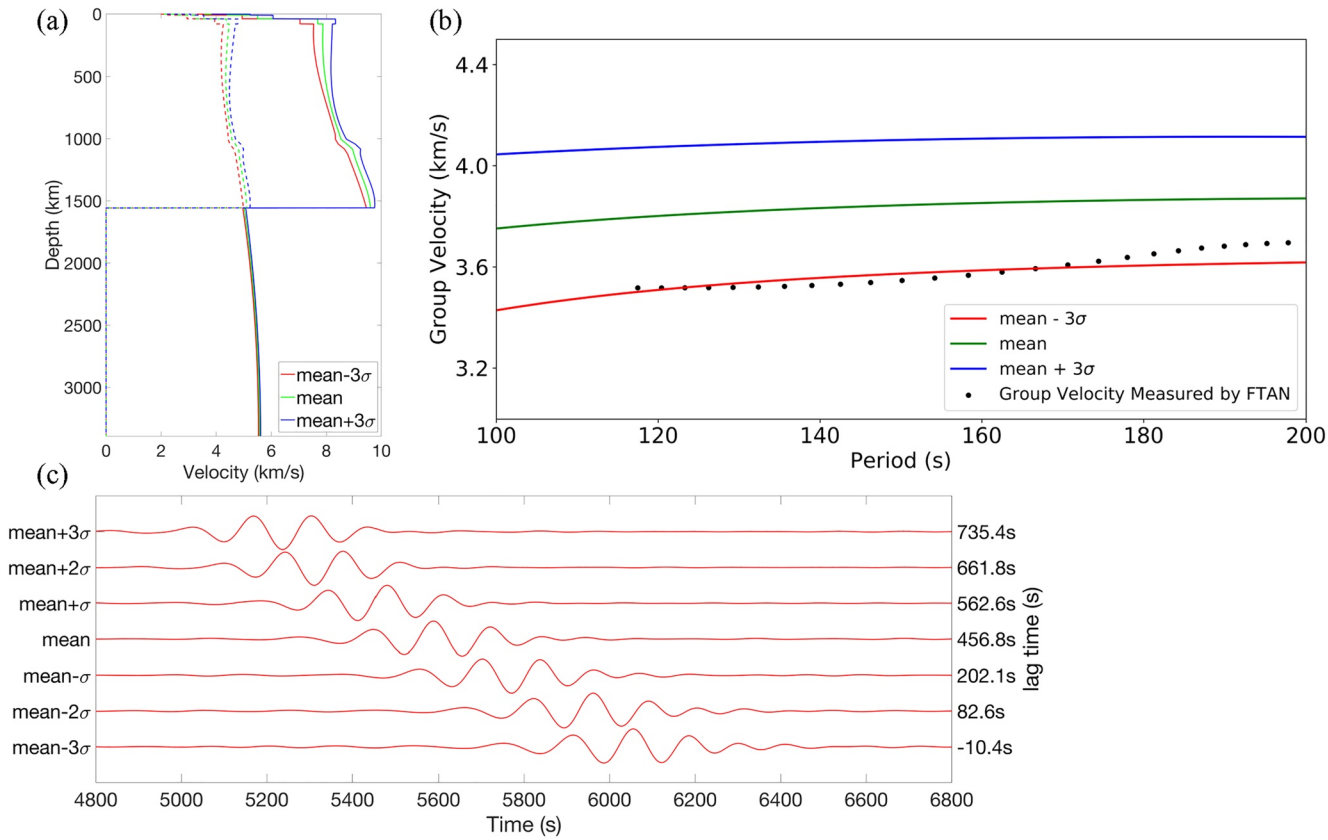

Figure 2. (a) Probabilistic inversion of the Martian velocity models in Stähler et al. (2021). The velocity models range from 3 standard deviations lower to 3 standard deviations higher than the mean velocity. (b) The group dispersion curves for different velocity models shown in (a) (solid lines) and the group velocities measured by frequency-time analysis (FTAN) of Figure 1h (black dots). (c) Synthetic seismograms filtered between 0.005 and 0.01 Hz for different velocity models shown in (a). The lag time is the cross-correlation time shift between the synthetic seismograms and the stacked vertical-component autocorrelation shown in Figure 1h. The positive lag time means that the observed R_2 phase propagates slower than the synthetics and vice versa.

Supporting Information S1) increases the correlation coefficients and reduces the absolute correlation time shifts between the observed and synthetic R_2 waveforms by a factor of 5 (Figure 3f). The model perturbation between the starting and final velocity models is shown in Figure S13 in Supporting Information S1. Figures S14 and S15 in Supporting Information S1 show that our final model can fit the body wave traveltime picks derived using different picking methods (Stähler et al., 2021).

The S-wave low-velocity zone (LVZ), extending to ~400 km depth, is clearly observed on the Monte Carlo inverted S-wave velocity model (Figure 3b), but the S-wave velocity has been increased compared to the starting model at depths >200 km and is reduced at depths <200 km (Figure S13a in Supporting Information S1). Geophysical modeling indicates that the S-wave LVZ may reach depths from 400 to 600 km (Khan et al., 2021), and has been predicted from laboratory measurement of seismic velocity for several representative Martian upper mantle compositions (Xu et al., 2021). The S-wave LVZ is thought to result from the steep thermal gradient in the Martian lithosphere arising from the thick conductive mantle (Khan et al., 2021). Moreover, a weak S-wave shadow zone is observed in an epicentral distances range from ~40 to 60°, providing independent evidence to support the presence of an S-wave LVZ within the Martian lithosphere (Giardini et al., 2020; Khan et al., 2021; Knapmeyer-Endrun & Kawamura, 2020). No equivalent LVZ is required in the upper mantle P-wave model (Figure 3a) as P-wave velocity is much less sensitive to temperature (Khan et al., 2021).

4. Conclusion

We applied the autocorrelation method to the InSight continuous vertical-component seismic data to provide the R_2 Rayleigh waves that propagate around Mars for one cycle. The R_2 surface waves are identified at ~6,000 s

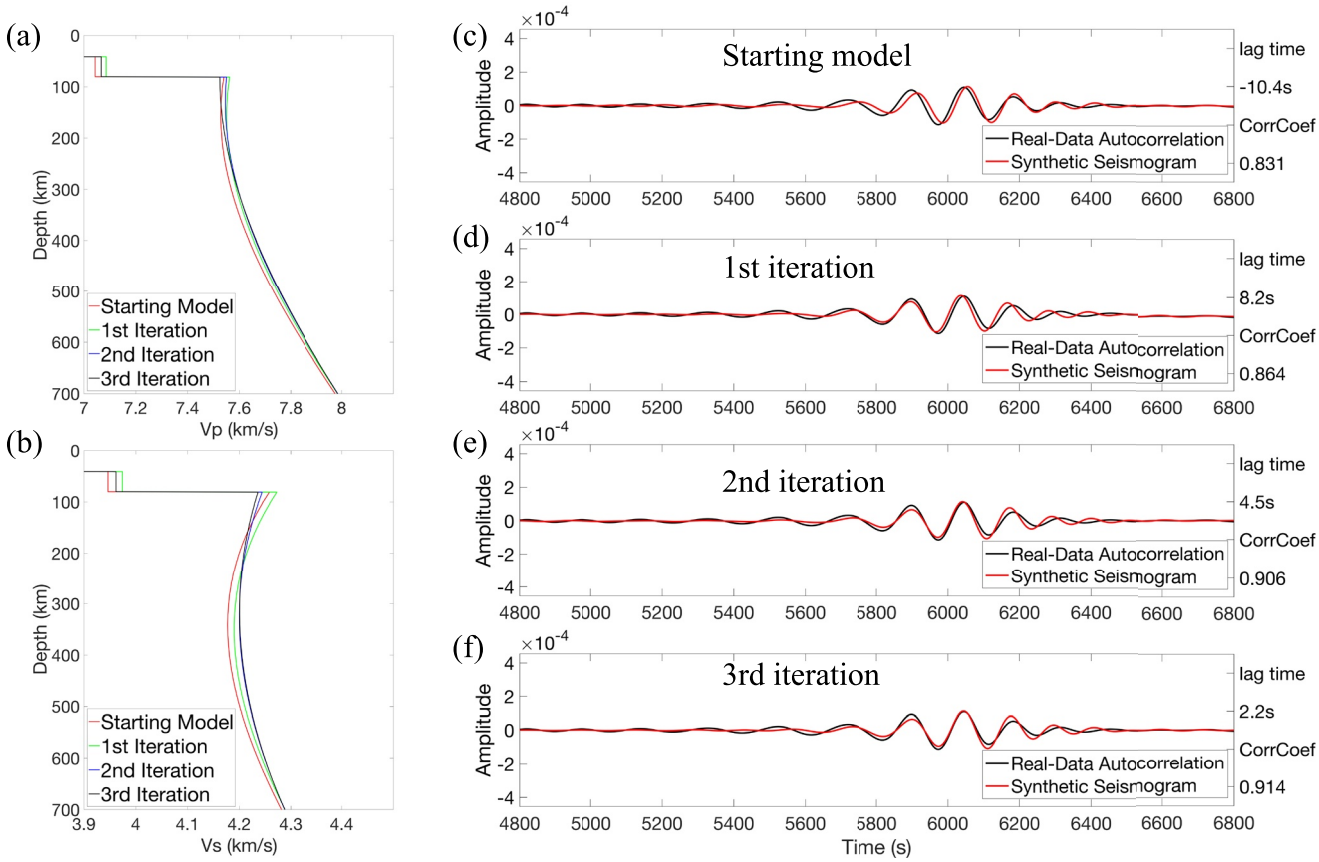

Figure 3. P- and S-wave velocity models of the Martian upper mantle (40–700 km) updated during the Monte Carlo inversion are shown in (a, b) respectively. The red curve is the mean-3σ model in Stähler et al. (2021). Comparisons between the synthetic R_2 waveforms and real-data autocorrelation (Figure 1h) filtered between 0.005 and 0.01 Hz for the starting velocity model (The red model in (a, b)) and the velocity models after first (The green model in (a, b)), second (The blue model in (a, b)) and third (The black model in (a, b)) iteration are shown in (c–f). The correlation time shifts and correlation coefficients between synthetic and observed R_2 waveforms are listed at the right side of (c–f). Positive lag time means that the observed R_2 phase propagates slower than synthetics and vice versa.

in the autocorrelations in the frequency band 0.005–0.01 Hz (Figure 1). Comparing synthetic group dispersion curves (Figure 2b) and seismograms (Figure 2c) from a set of Martian velocity models in Figure 2a, we found that the upper mantle shear velocity structure is slower than the mean model derived from the joint inversion of multiple geophysical datasets (Stähler et al., 2021). A Monte Carlo inversion was employed to perturb the velocity model 3 standard deviations lower than the mean velocity model of Stähler et al. (2021). We obtained a model that better fits the observed R_2 Rayleigh waves than the starting model (Figure 3f). The R_2 model is different from the mean-3σ model in Stähler et al. (2021) with velocities slower at depths <200 km and faster at depths >200 km (Figures 3b and S13a in Supporting Information S1). The S-wave LVZ extends to a depth of ~400 km in the Martian upper mantle (Figure 3b), consistent with the S-body wave shadow zone observed in the Marsquake data (Giardini et al., 2020; Khan et al., 2021; Knapmeyer-Endrun & Kawamura, 2020), geophysical inversion (Khan et al., 2021), and high-pressure laboratory experiments (Xu et al., 2021).

Data Availability Statement

The seismic data of the Interior Exploration Using Seismic Investigations, Geodesy and Heat Transport (InSight) mission (InSight Mars SEIS Data Service, 2019; https://www.iris.edu/hq/sis/insight) used in this study were downloaded by a BREQ_FAST request from the Incorporated Research Institutions for Seismology (IRIS) data center (https://ds.iris.edu/ds/nodes/dmc/forms/breqfast-request/). The open-source package SEISglitch (Scholz et al., 2020) can be installed in Python through the following instructions (https://seisglitch.readthedocs.io/en/latest/). The synthetic group dispersion curves of spherically symmetric velocity models were calculated by Computer Programs in Seismology (CPS) (Herrmann, 2013). The direct solution method (DSM) software

(Kawai et al., 2006) can be accessed at the following URL (http://www-solid.eps.s.u-tokyo.ac.jp/~dsm/software/software.htm).

Acknowledgments
This research is supported by the Department of Earth, Environmental and Planetary Sciences at Rice University. We thank Robert Geller and Kenji Kawai from The University of Tokyo for providing the detailed instructions of the direct solution method (DSM) software (Kawai et al., 2006) to calculate the synthetic Green's functions. We were schooled in the instrumental noise of the Seismic Experiment for Interior Structure (SEIS) instrument by Doyeon Kim, Mark Panning, Martin Schimmel, Paul Davis and other members of the InSight group. We appreciate the constructive comments from Editor Germán A. Prieto, Associate Editor Thomas Dylan Mikesell, Reviewer Bob Nowack and another anonymous reviewer to improve the manuscript.

References

Banerdt, W. B., Smrekar, S. E., Banfield, D., Giardini, D., Golombek, M., Johnson, C. L., et al. (2020). Initial results from the InSight mission on Mars. *Nature Geoscience*, *13*(3), 183–189. https://doi.org/10.1038/s41561-020-0544-y

Barkaoui, S., Lognonné, P., Kawamura, T., Stutzmann, É., Seydoux, L., de Hoop, M. V., et al. (2021). Anatomy of continuous Mars SEIS and pressure data from unsupervised learning. *Bulletin of the Seismological Society of America*, *111*(6), 2964–2981. https://doi.org/10.1785/0120210095

Bensen, G. D., Ritzwoller, M. H., Barmin, M. P., Levshin, A. L., Lin, F., Moschetti, M. P., et al. (2007). Processing seismic ambient noise data to obtain reliable broad-band surface wave dispersion measurements. *Geophysical Journal International*, *169*(3), 1239–1260. https://doi.org/10.1111/j.1365-246X.2007.03374.x

Berg, E. M., Lin, F. C., Allam, A., Qiu, H., Shen, W., & Ben-Zion, Y. (2018). Tomography of Southern California via Bayesian joint inversion of Rayleigh wave ellipticity and phase velocity from ambient noise cross-correlations. *Journal of Geophysical Research: Solid Earth*, *123*(11), 9933–9949. https://doi.org/10.1029/2018JB016269

Böse, M., Stähler, S. C., Deichmann, N., Giardini, D., Clinton, J., Lognonné, P., et al. (2021). Magnitude scales for Marsquakes calibrated from InSight data. *Bulletin of the Seismological Society of America*, *111*(6), 3003–3015. https://doi.org/10.1785/0120210045

Cai, A., Qiu, H., & Niu, F. (2022). Semi-supervised surface wave tomography with Wasserstein cycle-consistent GAN: Method and application to Southern California plate boundary region. *Journal of Geophysical Research: Solid Earth*, *127*(3), e2021JB023598. https://doi.org/10.1029/2021jb023598

Ceylan, S., Clinton, J. F., Giardini, D., Böse, M., Charalambous, C., van Driel, M., et al. (2021). Companion guide to the marsquake catalog from InSight, Sols 0–478: Data content and non-seismic events. *Physics of the Earth and Planetary Interiors*, *310*, 106597. https://doi.org/10.1016/j.pepi.2020.106597

Clayton, R. W. (2020). Imaging the subsurface with ambient noise autocorrelations. *Seismological Research Letters*, *91*(2A), 930–935. https://doi.org/10.1785/0220190272

Clinton, J. F., Ceylan, S., van Driel, M., Giardini, D., Stähler, S. C., Böse, M., et al. (2021). The marsquake catalogue from InSight, sols 0–478. *Physics of the Earth and Planetary Interiors*, *310*, 106595. https://doi.org/10.1016/j.pepi.2020.106595

Compaire, N., Margerin, L., Garcia, R. F., Pinot, B., Calvet, M., Orhand-Mainsant, G., et al. (2021). Autocorrelation of the ground vibrations recorded by the SEIS-InSight seismometer on Mars. *Journal of Geophysical Research: Planets*, *126*(4), 1–20. https://doi.org/10.1029/2020JE006498

Deng, S., & Levander, A. (2020). Autocorrelation reflectivity of Mars. *Geophysical Research Letters*, *47*(16), e2020GL089630. https://doi.org/10.1029/2020GL089630

Erhan, E., & Nowack, R. L. (2020). Application of non-stationary iterative time-domain deconvolution. *Studia Geophysica et Geodaetica*, *64*(1), 76–99. https://doi.org/10.1007/s11200-019-1165-z

Feng, J., Yao, H., Poli, P., Fang, L., Wu, Y., & Zhang, P. (2017). Depth variations of 410 km and 660 km discontinuities in eastern North China Craton revealed by ambient noise interferometry. *Geophysical Research Letters*, *44*(16), 8328–8335. https://doi.org/10.1002/2017GL074263

Feng, J., Yao, H., Wang, Y., Poli, P., & Mao, Z. (2021). Segregated oceanic crust trapped at the bottom mantle transition zone revealed from ambient noise interferometry. *Nature Communications*, *12*(1), 1–8. https://doi.org/10.1038/s41467-021-22853-2

Geller, R. J., & Takeuchi, N. (1995). A new method for computing highly accurate DSM synthetic seismograms. *Geophysical Journal International*, *123*(2), 449–470. https://doi.org/10.1111/j.1365-246X.1995.tb06865.x

Giardini, D., Lognonné, P., Banerdt, W., Pike, W., Christensen, U., Ceylan, S., et al. (2020). The seismicity of Mars. *Nature Geoscience*, *13*(3), 205–212. https://doi.org/10.1038/s41561-020-0539-8

Gorbatov, A., Saygin, E., & Kennett, B. L. N. (2013). Crustal properties from seismic station autocorrelograms. *Geophysical Journal International*, *192*(2), 861–870. https://doi.org/10.1093/gji/ggs064

Hable, S., Sigloch, K., Stutzmann, E., Kiselev, S., & Barruol, G. (2019). Tomography of crust and lithosphere in the Western Indian Ocean from noise cross-correlations of land and ocean bottom seismometers. *Geophysical Journal International*, *219*(2), 924–944. https://doi.org/10.1093/gji/ggz333

Haned, A., Stutzmann, E., Schimmel, M., Kiselev, S., Davaille, A., & Yelles-Chaouche, A. (2016). Global tomography using seismic hum. *Geophysical Journal International*, *204*(2), 1222–1236. https://doi.org/10.1093/gji/ggv516

Hannemann, K., Papazachos, C., Ohrnberger, M., Savvaidis, A., Anthymidis, M., & Lontsi, A. M. (2014). Three-dimensional shallow structure from high-frequency ambient noise tomography: New results for the Mygdonia basin-Euroseistest area, northern Greece. *Journal of Geophysical Research: Solid Earth*, *119*(6), 4979–4999. https://doi.org/10.1002/2013JB010914

Herrmann, R. B. (2013). Computer programs in seismology: An evolving tool for instruction and research. *Seismological Research Letters*, *84*(6), 1081–1088. https://doi.org/10.1785/0220110096

InSight Mars SEIS Data Service. (2019). SEIS raw data, Insight Mission. IPGP, JPL, CNES, ETHZ, ICL, MPS, ISAE-Supaero, LPG, MFSC. https://doi.org/10.18715/SEIS.INSIGHT.XB_2016

Kawai, K., Takeuchi, N., & Geller, R. J. (2006). Complete synthetic seismograms up to 2 Hz for transversely isotropic spherically symmetric media. *Geophysical Journal International*, *164*(2), 411–424. https://doi.org/10.1111/j.1365-246X.2005.02829.x

Kennett, B. L. N. (2015). Lithosphere-asthenosphere P-wave reflectivity across Australia. *Earth and Planetary Science Letters*, *431*, 225–235. https://doi.org/10.1016/j.epsl.2015.09.039

Khan, A., Ceylan, S., van Driel, M., Giardini, D., Lognonné, P., Samuel, H., et al. (2021). Upper mantle structure of Mars from InSight seismic data. *Science*, *373*(6553), 434–438. https://doi.org/10.1126/science.abf2966

Kim, D., Davis, P., Lekić, V., Maguire, R., Compaire, N., Schimmel, M., et al. (2021). Potential pitfalls in the analysis and structural interpretation of Mars' seismic data from InSight. *Bulletin of the Seismological Society of America*, *111*(6), 1–21. https://doi.org/10.1785/0120210123

Knapmeyer, M., Stähler, S. C., Daubar, I., Forget, F., Spiga, A., Pierron, T., et al. (2021). Seasonal seismic activity on Mars. *Earth and Planetary Science Letters*, *576*, 117171. https://doi.org/10.1016/j.epsl.2021.117171

Knapmeyer-Endrun, B., & Kawamura, T. (2020). NASA's InSight mission on Mars—First glimpses of the planet's interior from seismology. *Nature Communications*, *11*(1), 1–4. https://doi.org/10.1038/s41467-020-15251-7

Knapmeyer-Endrun, B., Panning, M. P., Bissig, F., Joshi, R., Khan, A., Kim, D., et al. (2021). Thickness and structure of the Martian crust from InSight seismic data. *Science*, *373*(6553), 438–443. https://doi.org/10.1126/science.abf8966

Levshin, A., Ratnikova, L., & Berger, J. (1992). Peculiarities of surface-wave propagation across central Eurasia. *Bulletin of the Seismological Society of America*, *82*(6), 2464–2493. https://doi.org/10.1785/bssa0820062464

Li, G., Niu, F., Yang, Y., & Xie, J. (2018). An investigation of time-frequency domain phase-weighted stacking and its application to phase-velocity extraction from ambient noise's empirical Green's functions. *Geophysical Journal International*, *212*(2), 1143–1156. https://doi.org/10.1093/gji/ggx448

Li, H., Li, S., Song, X. D., Gong, M., Li, X., & Jia, J. (2012). Crustal and uppermost mantle velocity structure beneath northwestern China from seismic ambient noise tomography. *Geophysical Journal International*, *188*(1), 131–143. https://doi.org/10.1111/j.1365-246X.2011.05205.x

Li, H., Xu, J., Chen, X., Sun, H., Zhang, M., & Zhang, L. (2020). Extracting long-period surface waves and free oscillations using ambient noise recorded by global distributed superconducting gravimeters. *Seismological Research Letters*, *91*(4), 2234–2246. https://doi.org/10.1785/0220190166

Li, J., Beghein, C., Wookey, J., Davis, P., Lognonné, P., Schimmel, M., et al. (2022). Evidence for crustal seismic anisotropy at the InSight lander site. *Earth and Planetary Science Letters*, *593*, 117654. https://doi.org/10.1016/j.epsl.2022.117654

Lin, F. C., Tsai, V. C., & Schmandt, B. (2014). 3-D crustal structure of the western United States: Application of Rayleigh-wave ellipticity extracted from noise cross-correlations. *Geophysical Journal International*, *198*(2), 656–670. https://doi.org/10.1093/gji/ggu160

Lognonné, P., Banerdt, W., Pike, W. T., Giardini, D., Christensen, U., Garcia, R. F., et al. (2020). Constraints on the shallow elastic and anelastic structure of Mars from InSight seismic data. *Nature Geoscience*, *13*(3), 213–220. https://doi.org/10.1038/s41561-020-0536-y

Lognonné, P., Banerdt, W. B., Giardini, D., Pike, W. T., Christensen, U., Laudet, P., et al. (2019). SEIS: Insight's seismic experiment for internal structure of Mars. *Space Science Reviews*, *215*(1), 12. https://doi.org/10.1007/s11214-018-0574-6

Miao, W., Niu, F., Li, G., & Levander, A. (2022). Sedimentary and crustal structure of the US Gulf Coast revealed by Rayleigh wave and teleseismic P coda data with implications for continent rifting. *Earth and Planetary Science Letters*, *577*, 117257. https://doi.org/10.1016/j.epsl.2021.117257

Nguyen, L. C., Levander, A., Niu, F., Morgan, J., & Li, G. (2022). Seismic evidence for lithospheric boudinage and its implications for continental rifting. *Geology*, *50*(9), 986–990. https://doi.org/10.1130/g50046.1

Nishida, K., Montagner, J. P., & Kawakatsu, H. (2009). Global surface wave tomography using seismic hum. *Science*, *326*(5949), 112. https://doi.org/10.1126/science.1176389

Oren, C., & Nowack, R. L. (2017). Seismic body-wave interferometry using noise autocorrelations for crustal structure. *Geophysical Journal International*, *208*(1), 321–332. https://doi.org/10.1093/gji/ggw394

Pan, Y., Xia, J., Xu, Y., Xu, Z., Cheng, F., Xu, H., & Gao, L. (2016). Delineating shallow S-wave velocity structure using multiple ambient-noise surface-wave methods: An example from Western Junggar, China. *Bulletin of the Seismological Society of America*, *106*(2), 327–336. https://doi.org/10.1785/0120150014

Qiu, H., Hillers, G., & Ben-Zion, Y. (2020). Temporal changes of seismic velocities in the San Jacinto Fault zone associated with the 2016 Mw 5.2 Borrego Springs earthquake. *Geophysical Journal International*, *220*(3), 1536–1554. https://doi.org/10.1093/gji/ggz538

Qiu, H., Lin, F. C., & Ben-Zion, Y. (2019). Eikonal tomography of the Southern California plate boundary region. *Journal of Geophysical Research: Solid Earth*, *124*(9), 9755–9779. https://doi.org/10.1029/2019JB017806

Qiu, H., Niu, F., & Qin, L. (2021). Denoising surface waves extracted from ambient noise recorded by 1-D linear array using three-station interferometry of direct waves. *Journal of Geophysical Research: Solid Earth*, *126*(8), e2021JB021712. https://doi.org/10.1029/2021JB021712

Schimmel, M., & Gallart, J. (2007). Frequency-dependent phase coherence for noise suppression in seismic array data. *Journal of Geophysical Research*, *112*(4), 1–14. https://doi.org/10.1029/2006JB004680

Schimmel, M., Stutzmann, E., & Gallart, J. (2011). Using instantaneous phase coherence for signal extraction from ambient noise data at a local to a global scale. *Geophysical Journal International*, *184*(1), 494–506. https://doi.org/10.1111/j.1365-246X.2010.04861.x

Schimmel, M., Stutzmann, E., Lognonné, P., Compaire, N., Davis, P., Drilleau, M., et al. (2021). Seismic noise autocorrelations on Mars. *Earth and Space Science*, *8*(6), 1–22. https://doi.org/10.1029/2021EA001755

Schimmel, M., Stutzmann, E., & Ventosa, S. (2018). Low-frequency ambient noise autocorrelations: Waveforms and normal modes. *Seismological Research Letters*, *89*(4), 1488–1496. https://doi.org/10.1785/0220180027

Scholz, J. R., Widmer-Schnidrig, R., Davis, P., Lognonné, P., Pinot, B., Garcia, R. F., et al. (2020). Detection, analysis, and removal of glitches from InSight's seismic data from Mars. *Earth and Space Science*, *7*(11), e2020EA001317. https://doi.org/10.1029/2020EA001317

She, Y., Yao, H., Yang, H., Wang, J., & Feng, J. (2022). Constraining the depth extent of low-velocity zone along the Chenghai Fault by dense array ambient noise interferometry and horizontal-to-vertical spectral ratio. *Tectonophysics*, *827*, 229265. https://doi.org/10.1016/j.tecto.2022.229265

Shen, W., Ritzwoller, M. H., & Schulte-Pelkum, V. (2013). A 3-D model of the crust and uppermost mantle beneath the Central and Western US by joint inversion of receiver functions and surface wave dispersion. *Journal of Geophysical Research: Solid Earth*, *118*(1), 262–276. https://doi.org/10.1029/2012JB009602

Shirzad, T., & Shomali, Z. H. (2014). Shallow crustal radial anisotropy beneath the Tehran basin of Iran from seismic ambient noise tomography. *Physics of the Earth and Planetary Interiors*, *231*, 16–29. https://doi.org/10.1016/j.pepi.2014.04.001

Stähler, S. C., Khan, A., Bruce Banerdt, W., Lognonné, P., Giardini, D., Ceylan, S., et al. (2021). Seismic detection of the Martian core. *Science*, *373*(6553), 443–448. https://doi.org/10.1126/science.abi7730

Stutzmann, E., Schimmel, M., Lognonné, P., Horleston, A., Ceylan, S., van Driel, M., et al. (2021). The polarization of ambient noise on Mars. *Journal of Geophysical Research: Planets*, *126*(1), 1–27. https://doi.org/10.1029/2020JE006545

Suemoto, Y., Ikeda, T., & Tsuji, T. (2020). Temporal variation and frequency dependence of seismic ambient noise on Mars from polarization analysis. *Geophysical Research Letters*, *47*(13), 1–9. https://doi.org/10.1029/2020GL087123

Takeuchi, N., Geller, R. J., & Cummins, P. R. (1996). Highly accurate P-SV complete synthetic seismograms using modified DSM operators. *Geophysical Research Letters*, *23*(10), 1175–1178. https://doi.org/10.1029/96GL00973

Xie, J., & Ni, S. (2019). Imaging 3D upper-mantle structure with autocorrelation of seismic noise recorded on a transportable single station. *Seismological Research Letters*, *90*(2 A), 708–715. https://doi.org/10.1785/0220180260

Xie, J., Yang, Y., & Luo, Y. (2020). Improving cross-correlations of ambient noise using an rms-ratio selection stacking method. *Geophysical Journal International*, *222*(2), 989–1002. https://doi.org/10.1093/gji/ggaa232

Xu, F., Siersch, N. C., Gréaux, S., Rivoldini, A., Kuwahara, H., Kondo, N., et al. (2021). Low velocity zones in the Martian upper mantle highlighted by sound velocity measurements. *Geophysical Research Letters*, *48*(19), e2021GL093977. https://doi.org/10.1029/2021gl093977

Yan, P., Li, Z., Li, F., Yang, Y., & Hao, W. (2019). Antarctic ice-sheet structures retrieved from P-wave coda autocorrelation method and comparisons with two other single-station passive seismic methods. *Journal of Glaciology*, *66*(255), 153–165. https://doi.org/10.1017/jog.2019.95

Yao, H., Beghein, C., & Van Der Hilst, R. D. (2008). Surface wave array tomography in SE Tibet from ambient seismic noise and two-station analysis—II. Crustal and upper-mantle structure. *Geophysical Journal International*, *173*(1), 205–219. https://doi.org/10.1111/j.1365-246X.2007.03696.x

Yao, H., van der Hilst, R. D., & de Hoop, M. V. (2006). Surface-wave array tomography in SE Tibet from ambient seismic noise and two-station analysis—I. Phase velocity maps. *Geophysical Journal International*, *166*(2), 732–744. https://doi.org/10.1111/j.1365-246X.2006.03028.x

Yilmaz, Ö. (2001). Seismic data analysis. *Seismic Data Analysis*, *10*. https://doi.org/10.1190/1.9781560801580

Zeng, X., Lancelle, C., Thurber, C., Fratta, D., Wang, H., Lord, N., et al. (2017). Properties of noise cross-correlation functions obtained from a distributed acoustic sensing array at Garner Valley, California. *Bulletin of the Seismological Society of America*, *107*(2), 603–610. https://doi.org/10.1785/0120160168

Zhang, Y., Yao, H., Yang, H. Y., Cai, H. T., Fang, H., Xu, J., et al. (2018). 3-D crustal shear-wave velocity structure of the Taiwan strait and Fujian, SE China, revealed by ambient noise tomography. *Journal of Geophysical Research: Solid Earth*, *123*(9), 8016–8031. https://doi.org/10.1029/2018JB015938